Nuclear Engineering and Technology 53 (2021) 583–591

Contents lists available at ScienceDirect

Nuclear Engineering and Technology

journal homepage: www.elsevier.com/locate/net

Original Article

Fabrication and thermal conductivity of CeO_2–Ce_3Si_2 composite

Jungsu Ahn, Gyeonghun Kim, Yunsong Jung, Sangjoon Ahn*

Department of Nuclear Engineering, Ulsan National Institute of Science and Technology, Ulju, Ulsan, 44919, Republic of Korea

ARTICLE INFO

Article history:
Received 31 January 2020
Received in revised form
27 June 2020
Accepted 12 July 2020
Available online 25 July 2020

Keywords:
Cerium oxide
Cerium silicide
Composite
Spark plasma sintering
Thermal conductivity

ABSTRACT

Various compositions of CeO_2–Ce_3Si_2 (0, 10, 30, 50, and 100 wt%Ce_3Si_2) composites were fabricated using conventional sintering and spark plasma sintering. Lower relative density, enhanced interdiffusion of oxygen and silicon, and silicide agglomerations from the congruent melting of Ce_3Si_2 at 1390 °C were only observed from conventionally-sintered pellets. Thermal conductivity of spark plasma sintered CeO_2–Ce_3Si_2 composites was calculated from the measured thermal diffusivity, specific heat, and density, which exhibited dense (>90 %TD) and homogeneous microstructure. The composite with 50 wt%Ce_3Si_2 exhibited 55% higher thermal conductivity than CeO_2 at 500 °C, and 81% higher at 1000 °C.

1. Introduction

Autonomous, Transportable, On-demand reactor-Module or '*ATOM*', is a conceptual soluble-boron-free small modular water-cooled reactor that enables passive daily load following operation (PDLFO) by autonomous frequency control, which requires lower fuel temperature than conventional LWRs to obtain less negative fuel temperature coefficient (FTC) [1]. UO_2-based composite fuel mixed with high thermal conductivity additives is considered for the reactor design to concurrently achieve enhanced fuel thermal conductivity, increased uranium loading, and reasonable corrosion resistance.

Increased uranium loading narrows the material selection down to uranium compounds such as UN, UC, and U_3Si_2, which all have higher thermal conductivity and fissile density than those of UO_2 [2–4]. Uranium sesquisilicide (U_3Si_2) was the first selected additive for this study owing to relatively better oxidation resistance among the uranium compounds, and it also has 4–8 times higher thermal conductivity and 16% higher fissile density compared to UO_2 [3].

Density-specific thermal conductivity database of the composite, which is the eventual goal of this study, is first required for candidate fuel compositions to examine the viability of the autonomous reactor design with UO_2–U_3Si_2 fuel. Surrogate material was, however, first tested to develop the fabrication process for the composite fuel while minimizing uranium-bearing waste generation. Among several surrogate elements, cerium (Ce) was selected since CeO_2 and Ce_3Si_2 have the same crystal structures with UO_2 and U_3Si_2, respectively [5–8]. The cerium compounds also have similar thermal conductivities and melting temperatures with their uranium counterparts [9–13]. In particular, the ratios between melting temperatures of CeO_2/Ce_3Si_2 (2490 °C/1390 °C) and UO_2/U_3Si_2 (2865 °C/1660 °C) were expected to be close enough to glimpse the sintering behavior of UO_2–U_3Si_2 composite.

In this study, various compositions of CeO_2-xCe_3Si_2 ($x = 0, 10, 30, 50$, and 100 wt%) composite pellets were fabricated using conventional sintering (CS) and spark plasma sintering (SPS) with varying sintering temperatures (1000, 1200, 1400, and 1600 °C). The resulted density and microstructure of CeO_2–Ce_3Si_2 composites were compared to optimize the parameters for each sintering method. The thermal conductivity of spark plasma sintered high density (>90 %TD) composite pellets were measured using laser flash analyzer (LFA) up to 1000 °C.

2. Material and methods

2.1. Sample preparation

Cerium sesquisilicide was synthesized utilizing high energy ball milling (HEBM) method, referring to G.A. Alanko et al. [12,14]. The starting materials were high purity elemental Ce powder (~45 μm, 99.9%, Avention) and Si powder (~1 μm, 99.9995%, Avention). Material handing and sintering was conducted in a glove box under an

* Corresponding author.
E-mail address: sjahn99@unist.ac.kr (S. Ahn).

https://doi.org/10.1016/j.net.2020.07.016

argon atmosphere with less than 10 ppm O_2 and H_2O to suppress rapid oxidation and ignition of flammable Ce and Ce_3Si_2 powders. The synthesis was performed using a planetary ball mill (Fritsch PUVERISETTE 6, Germany) with 5- and 10-mm diameter milling media in 80 ml ZrO_2 inert atmosphere milling vessel. The elemental Ce and Si powder were loaded into milling vessel with 3:2 M ratio, with milling media of 10:1 ball-to-powder ratio. The milling process was carried out at 550 rpm for 12 h, followed by 1 h milling and 5 min break. The milled powder attached to the vessel wall was collected by additional milling with acetone at 400 rpm for 30 min and the resulted mixture was vaporized to obtain Ce_3Si_2 powder. The microstructure and phase of the as-milled powder were characterized using scanning electron microscope (Quanta200 FEG SEM, FEI, USA) and X-ray diffraction (XRD, D/MAX-2500, Rigaku, Japan). It needs to be noted that the XRD samples were prepared in a bulk form of 1 mm high pellet, which was spark plasma sintered at 600 °C for 5 min, to address the flammability issue of Ce_3Si_2 powder in air.

2.2. Sintering

As-received CeO_2 powder (~1 μm, 99.9%, Avention) shown in Fig. 1 was homogeneously blended with 0/10/30/50/100 wt% of as-milled Ce_3Si_2 powder using 3d tubular mixer at 150 rpm for 30 min. For the CS of the composite, ~57 %TD green pellets were prepared from cold compacting the mixed powder with 300 MPa in 12.7 mm diameter stainless steel die for 1 min. The green pellets were then sintered using a tube furnace (Nabertherm GmbH, Germany) at various temperatures (1000, 1200, 1400, and 1600 °C) for 6 h under an Ar atmosphere; 5 °C/min ramping rates and alumina (Al_2O_3) crucible were adopted for all sintering temperatures. The SPS of the composite was carried out using DrSinter SPS-211LX. The mixed powder was loaded into 9.5 mm diameter graphite mold of which inside was wrapped with graphite foil to avoid sample-mold reaction, and then heated up to the same sintering temperatures with CS; however, with different ramping rate (80 °C/min), holding time (10 min), and atmosphere (vacuum), under 45 MPa of biaxial pressure. The SPS system temperature was monitored through a 0.5 mm diameter hole at the center of graphite mold using focused infrared pyrometer.

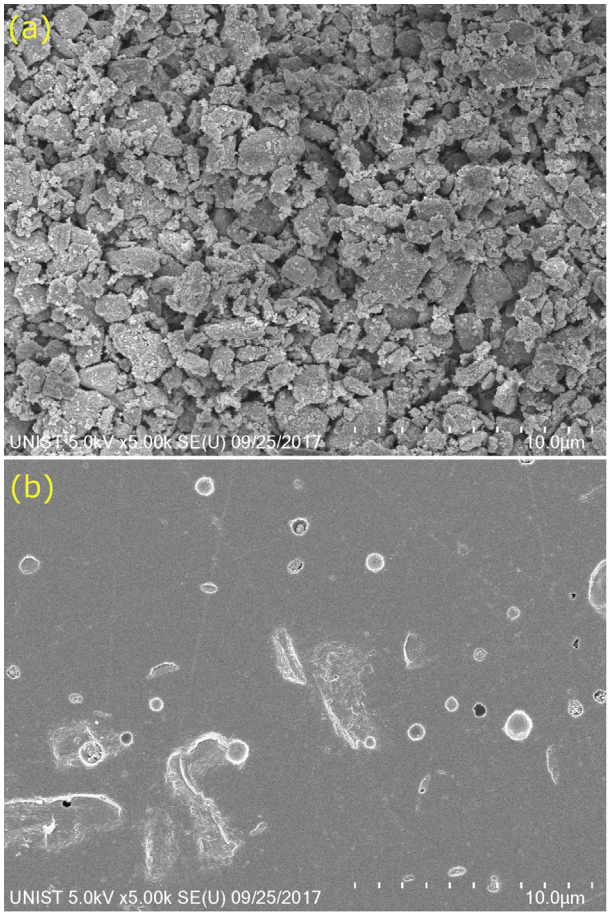

Fig. 1. SEM image of (a) as-received CeO_2 powder, (b) conventionally sintered CeO_2 pellet (1600 °C, 6 h).

As-fabricated composite pellet density was measured using the Archimedes immersion method with ethyl alcohol (C_2H_5OH), and validated with measured density with mass divided by measured volume. The pellet morphology was observed using an optical microscope (OM, DM2700 M, Leica, Japan) and SEM (SU8220, Hitachi, Japan). The phase characterization was carried out by energy dispersive spectrometry (EDS) and XRD (D8 advanced, Bruker AXS, USA) with 20–80° 2θ angle.

2.3. Thermal conductivity measurements

Thermal diffusivity and specific heat of the SPS pellets of CeO_2-$x$$Ce_3Si_2$ (x = 0, 10, 30, 50, and 100 wt%), sintered at 1000, 1200, and 1400 °C, were measured up to 1000 °C under an Ar atmosphere using LFA (LFA467HT, Netzsch, Germany); each measurement was repeated three times. The LFA samples were 9.8 mm in diameter and ~1.5 mm high, and graphite sprayed to increase Xenon laser absorptivity and emissivity. Thermal conductivity of the composite pellets was calculated from measured pellet density, average thermal diffusivity, and specific heat, using equation (1),

$$\lambda(T) = \alpha(T) \cdot C_P(T) \cdot \rho(T) \quad (1)$$

where λ is thermal conductivity, α is average thermal diffusivity, C_p is heat capacity, and ρ is measured density. Pellet density change during the measurement was tracked using a dilatometer (DIL-402C, Netzsch, Germany) and used to correct the measured density.

3. Results

3.1. Powder characterization

As-received CeO_2 powder with an average size of ~2 μm and conventionally sintered CeO_2 pellet at 1600 °C for 6 h are indicated at Fig. 1. The morphology of metallic Ce powder (spherical) and as-milled Ce_3Si_2 powder (arbitrary, 0.1–3 μm), and Ce_3Si_2 pellet are shown in Fig. 2. The XRD peaks of the starting materials, Ce and Si, and as-milled Ce_3Si_2 powder shown in Fig. 3 were identified referring to Inorganic Crystal Structure Database (ICSD) [15]; likely tetragonal Ce_3Si_2 with secondary off-stoichiometric Ce_5Si_4 and Ce_2O_3 phases. A few missing primary diffraction peaks of Ce_3Si_2 could be attributed to crystallographic texture of bulk XRD sample resulted from spark plasma sintering under high pressure.

3.2. Pellet characterization

Fig. 4 shows the XRD analysis of CeO_2 powder and CeO_2-30 wt% Ce_3Si_2 composites fabricated by CS and SPS. Both sintering methods yielded similar results which indicate the formation of Ce_2O_3, but much higher peak for CS.

The sintered pellet density was measured using Archimedes' principle, and the relative density for four different sintering

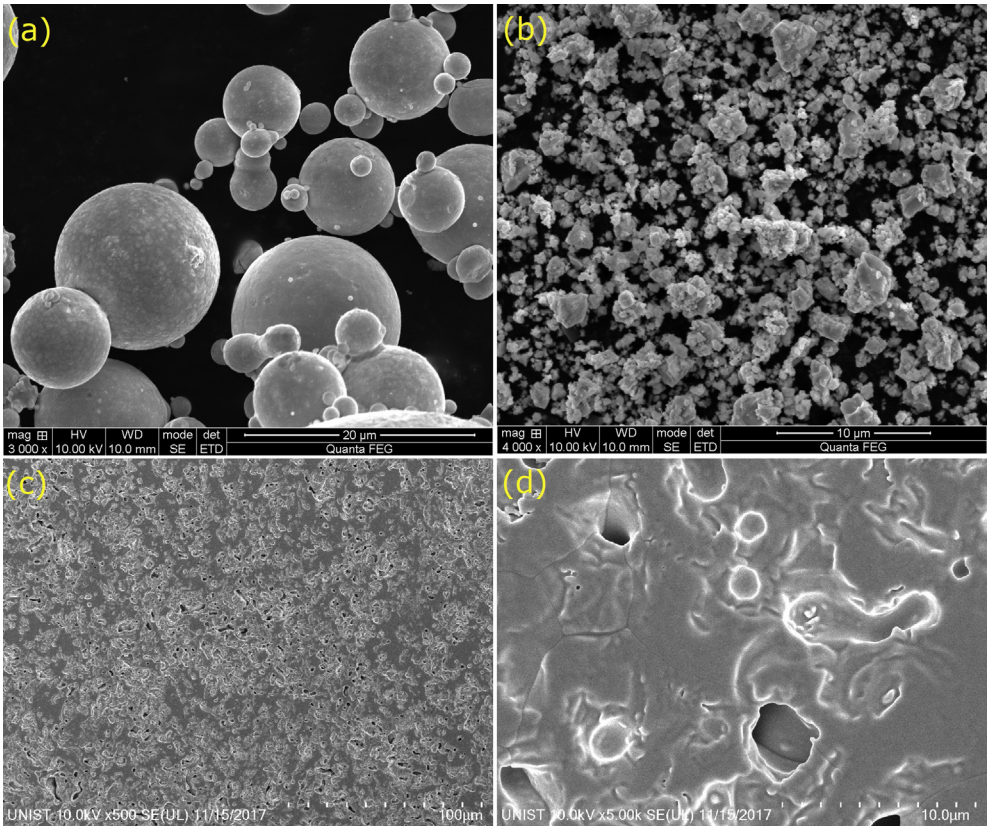

Fig. 2. SEM image of (a) as-received Ce metal powder, and (b) Ce_3Si_2 powder, (c) and (d) conventionally sintered Ce_3Si_2 pellet (1200 °C, 6 h).

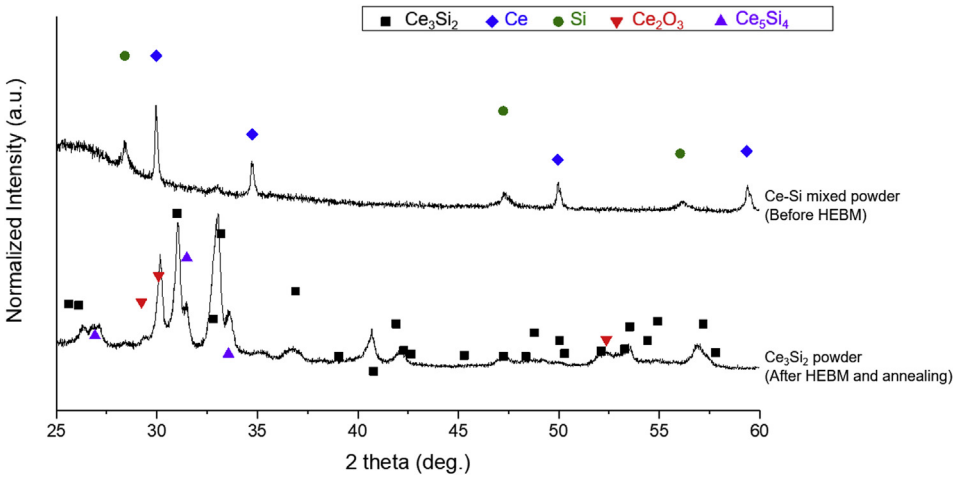

Fig. 3. XRD diffraction pattern for homogeneously mixrd Ce–Si powder and HEBM synthesized Ce_3Si_2 powder with 24 h annealing at 800 °C.

temperatures (1000, 1200, 1400, and 1600 °C) are displayed in Fig. 5; data for conventionally sintered 100 wt% Ce_3Si_2 pellet are not included due to partial melt, sequential loss of mixed powder from the mold. Spark plasma sintering always yielded higher density (83–96 %TD) pellets compared to CS at the same sintering temperature, and pellet densities were increasing monotonically with increasing sintering temperature for both methods. For CS pellets, however, density increase with elevated sintering temperature was remarkable, from ~62 %TD for 1000 °C to ~92%TD for 1600 °C, especially at high sintering temperature which seems to be the effect of liquid phase sintering. In contrast, sintering temperature effect for SPS tends to saturate at 1200 °C, especially for silicide-rich (>30 wt%Ce_3Si_2) pellets. For CS, single phase CeO_2 showed the highest relative density, while 10 wt%Ce_3Si_2 showed the lowest.

The OM and SEM images of the 30 wt%Ce_3Si_2 composite pellet sintered at 1600 °C are given in Fig. 6, which representatively shows the characteristic microstructure of CS pellets, bulk composite matrix with submillimeter metallic inclusions surrounded with interaction area, which are comprised of numerous submicron hexagonal particles. The EDS mapping on the inclusion (Fig. 7) shows silicon enrichment for the inclusion and depletion from the bulk. This metallic inclusions was rarely observed from the SPS

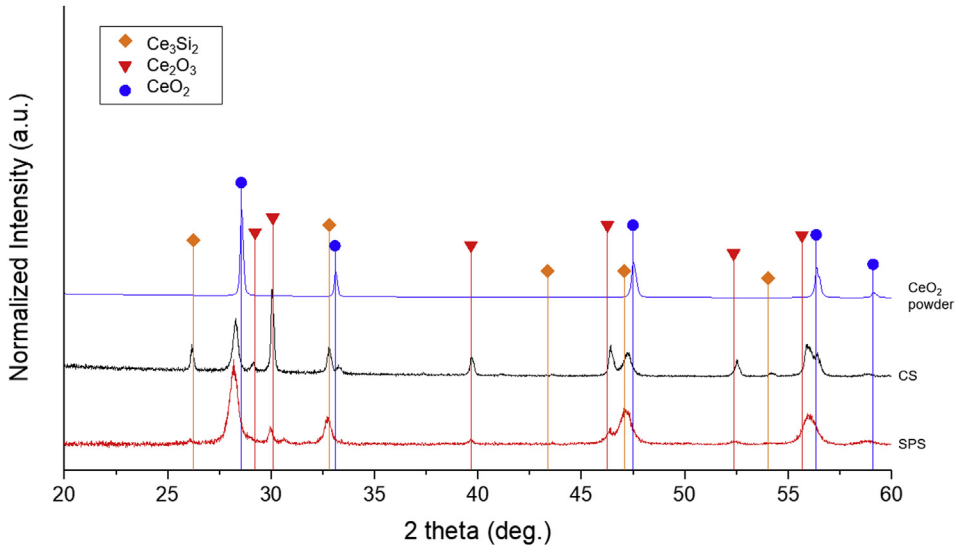

Fig. 4. XRD diffraction pattern for CeO_2-30 wt%Ce_3Si_2 pellets sintered by CS at 1600 °C for 6 h and SPS at 1400 °C for 10 min.

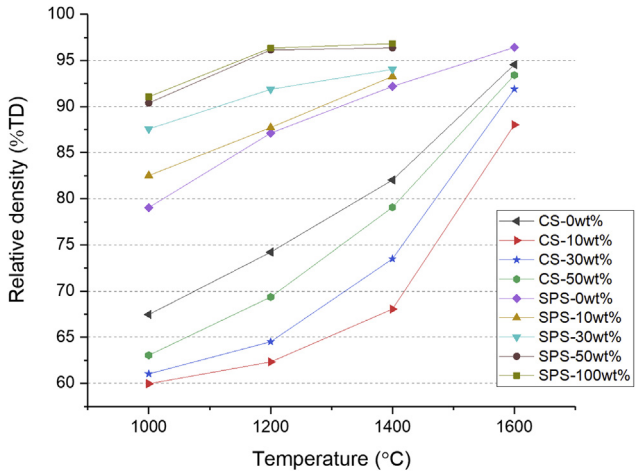

Fig. 5. Relative density of conventionally and spark plasma sintered composite pellets with varying sintering temperature and Ce_3Si_2 composition.

pellets; a rather homogeneous distribution of silicide within oxide matrix, almost without pores, is well shown in Fig. 8. The EDS mapping of CeO_2-30 wt%Ce_3Si_2 (Fig. 9) also shows clear phase boundary and limited oxygen presence in the SPS pellet in contrast to diffused phase boundary and near homogeneous oxygen distribution in the CS pellet. Both composite pellets sintered by CS and SPS method did not show distinct interaction layer between the interface of CeO_2 and Ce_3Si_2.

3.3. *Thermal conductivity of CeO_2–Ce_3Si_2 composites*

Thermal conductivity and specific heat capacity of the composites was only measured from the SPS pellets considering more homogeneous and dense microstructures shown in Figs. 8 and 9. The measured thermal conductivities of CeO_2-$x$$Ce_3Si_2$ ($x = 0$, 10, 30, 50, and 100 wt%) composites are summarized in Table 1. Thermal conductivities of CeO_2 (4.9 W/m-K) and Ce_3Si_2 (5.4 W/m-K) are similar at room temperature; however, with increasing temperature, increasing thermal conductivity of Ce_3Si_2 (8.3 W/m-K) reaches ~5.7 times higher value than that of CeO_2 (1.9 W/m-K) at 1000 °C, which well resembles the temperature dependency of UO_2 and U_3Si_2 thermal conductivities [3,16]. Enhanced thermal conductivity of the composites for high temperature regime (>300 °C) also can be confirmed from Fig. 10, even despite the higher relative density of CeO_2 pellet than those of composite pellets. Quantitative comparisons between thermal conductivities of the composites and CeO_2 are summarized in Table 2.

4. Discussion

From the XRD diffraction pattern shown in Fig. 4, Ce_2O_3 peaks, rather than CeO_2, were observed in both CS and SPS pellets. This reduction of the oxide was anticipated considering easily reducing enviornment of CeO_2 such as high temperature, oxidizing of Ce_xSi_y and the aforementioned sintering atmosphere, vacuum for SPS and argon for CS [17–19]. However, these reductive sintering conditions were unavoidable to not oxidize the silicide since the goal of this study was to quantify the thermal conductivity enhancement effect from Ce_3Si_2 addition.

In the standpoint of establishing the fabrication process for UO_2–U_3Si_2 composite, Fig. 5 shows four important points: (1) SPS pellets always exhibited higher relative density compared to CS, regardless of silicide composition and sintering temperature; (2) relatively low sintering temperature (~1400 °C) was enough for SPS to achieve high relative density (>90 %TD); (3) higher sintering temperature (>1600 °C) was required for CS to achieve the same level of high density; (4) for both sintering methods, higher relative density was achieved with higher silicide contents, perhaps largely indebted to high melting temperature of CeO_2 and low temperature densification of Ce_3Si_2 [20–24]. The reason for high density of SPS pellets might be not only the high sintering performance of SPS, but also the actual temperature is higher than the measured temperature. The radial temperature gradient from mold surface to center exists and the pyrometer measured only the mold surface temperature [25,26]. Even considering the fact above, however, SPS pellets already has fully compacted at 1200 °C of measured sintering temperature, which suggests that fact, the actual sintering temperature in SPS is higher than the measured temperature, has no significant effect of pellet density in this experiment.

Large silicon-rich inclusions, interaction area, and crack shown in Fig. 6(b) and Fig. 7 were discovered from all compositions of CS

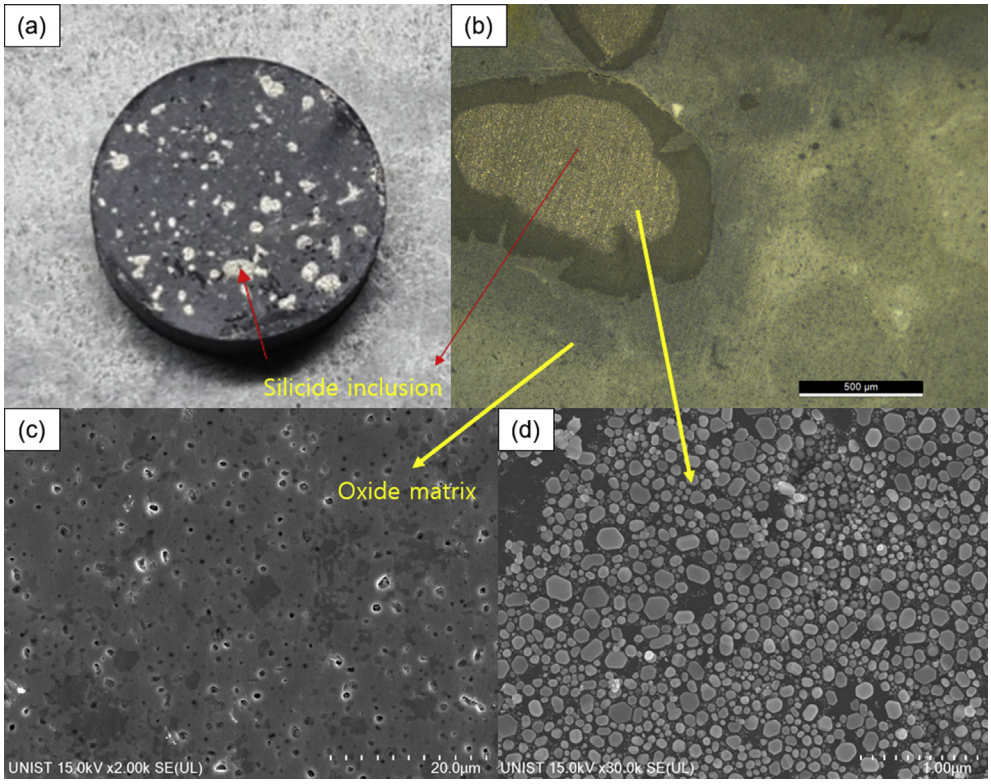

Fig. 6. Microstructure of CeO_2-30 wt%Ce_3Si_2 composites sintered by CS at 1600 °C for 6 h. (a) cross section of pellet, (b) OM image, (c) SEM image of oxide matrix, and (d) silicide inclusion.

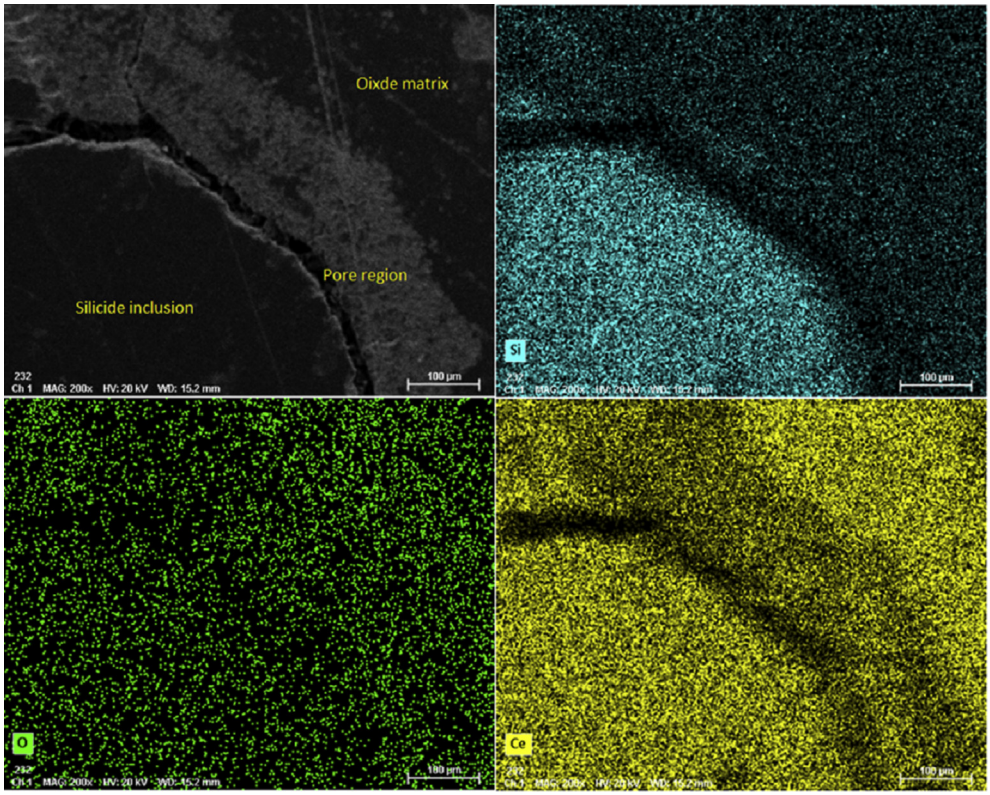

Fig. 7. EDS mapping image of CeO_2-30 wt%Ce_3Si_2 composites sintered by CS at 1600 °C for 6 h.

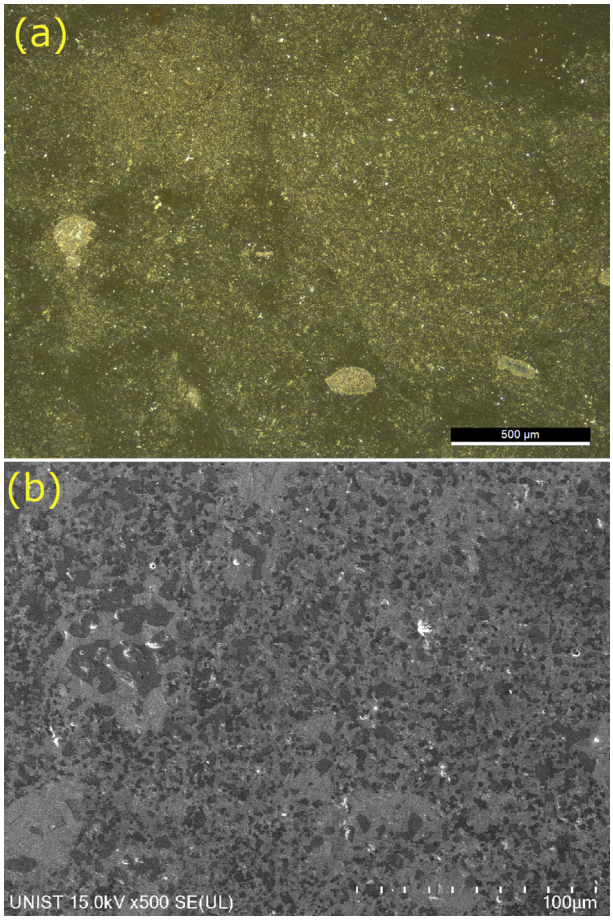

Fig. 8. Microstructure of CeO_2-30 wt%Ce_3Si_2 composite sintered by SPS at 1400 °C for 10 min. (a) OM image, and (b) SEM image.

pellets sintered at 1600 °C, which consisting of numerous hexagonal submicron precipitates as shown in Fig. 6(d). Smaller precipitate size than that of the starting Ce_3Si_2 powder may imply that their formation was by the congruent melting of Ce_3Si_2 at 1390 °C and its sequential agglomeration [7]. This type of complex microstructure such as inhomogeneous silicide agglomeration and 2nd phase formation in high temperature sintered CS pellets could be potential performance and safety issues for the UO_2—U_3Si_2 fuel, especially during daily load following operation incurring more frequent thermal cycling of the fuel. Differential thermal expansion coefficients of the silicide agglomeration, secondary phases, and the oxide bulk could facilitate additional fuel cracking, other than typical radial cracking in conventional UO_2 fuel [27,28]. This additional mode of cracking could decrease effective fuel thermal conductivity and increase stress concentration on zircaloy cladding via pellet-cladding mechanical interaction. The SPS pellets, on the contrary, relatively showed more homogeneous distribution of CeO_2 and Ce_3Si_2 as shown in Fig. 8, likely resulted from 36 times shorter holding time (10 min) at lower sintering temperature (1400 °C), compared to 6 h and 1600 °C for CS pellets.

Density-wise, despite the remarkable increase of CS pellet densities by the liquid phase sintering with increasing sintering temperature, obtained relative densities of 10 wt%Ce_3Si_2 composites are still below 90 %TD for all sintering temperatures. For 30 and 50 wt% composites, only the highest temperature (1600 °C) CS gives over 90 %TD. In contrast, 1200 °C SPS already achieved over 90 %TD, except 10 wt% pellets, which indicates the congruent melting issue at 1390 °C in CS can be avoided using SPS. Thus, thermal conductivity database of UO_2—U_3Si_2 composites can be more reliably constructed utilizing low temperature SPS, especially for silicide-rich (≥30 wt%) compositions.

Another superior characteristic of SPS, suppressed interdiffusion of oxygen and silicon between the two-phase boundary, can be designated from the EDS results shown in Fig. 9. Relatively enhanced interdiffusion of non-metallic elements in CS composites reaffirmed the decision to not measure the thermal conductivity of CS pellets with low relative density (<80 %TD) for lower sintering temperature (≤1400 °C) and the congruent melting for the high sintering temperature (1600 °C). However, conventional sintering will still be considered for the further study on uranium-bearing composite, since the congruent melting of U_3Si_2 occurs at 1660 °C and therefore less severe agglomeration and secondary phase formation are expected for UO_2—U_3Si_2 binary system.

Fig. 10 indicates that the thermal conductivity of the composites is actually lower than pure CeO_2 for low temperature region (<~250 °C). The cerium dioixde can be easily converted to CeO_{2-x} or Ce_2O_3 at reducible enviornment such as the presence of Ce_xSi_y nearby, which is verified by the Ce_2O_3 peak shown in Fig. 4. The thermal conductivity of CeO_2 is dominantly determined by the phonon scattering at the low temperature range. The oxygen vacancy from hypo-stoichiometry phase can interfere with phonon transfer, which resluted in lower thermal conductivity. The thermal conductivity tendency as Ce_3Si_2 fraction is flipped for all composites for high temperature region by the significantly higher thermal conductivity of Ce_3Si_2 itself, which collectively are a suitable characteristic as a nuclear fuel. Most notably, 50 wt%Ce_3Si_2 composite exhibited 55% higher value at 500 °C and 81% higher value at 1000 °C.

This thermal conductivity enhancement of the surrogate composites would be much more significant for UO_2—U_3Si_2 composites mainly due to two following reasons. First, the reduction of CeO_2 during the fabrication prohibited the thermal conductivity enhancement of the composites; however, UO_2 stoichiometry decrease under high temperature reductive environment is very limited in comparison to that of CeO_2 [17,29]. Second, U_3Si_2 has 11% higher density (12.2 g/cm^3) than UO_2 (10.96 g/cm^3), unlike 17% lower density of Ce_3Si_2 (5.97 g/cm^3) than that of CeO_2 (7.22 g/cm^3). This indicates that the thermal conductivity enhancement of the CeO_2—Ce_3Si_2 composites was determined by higher thermal conductivity of Ce_3Si_2 and the reduction of CeO_2. Additional thermal conductivity enhancement can thus be expected from UO_2—U_3Si_2 composites due to stoichiometric UO_2 and further increased density by silicide compositing.

5. Conclusion

Various compositions of non-radioactive surrogate composites, CeO_2-xCe_3Si_2 (x = 0, 10, 30, 50, and 100 wt%) were fabricated using conventional sintering and spark plasma sintering in order to effectively construct the thermal conductivity database of UO_2—U_3Si_2 nuclear fuel with minimum uranium-bearing waste generation. Thermal conductivity of the composites was measured from spark plasma sintered pellets due to their homogeneous microstructure and high relative density (>90%TD). Silicide agglomerations and enhanced interdiffusion of oxygen and silicon observed from conventionally-sintered pellets, which could be potential safety issue, were additional reasons to exclude the CS pellets from the in addition to their low relative densities. Based upon measured thermal conductivity of the surrogate, the UO_2—U_3Si_2 composites may be suitable candidates, since CeO_2-50 wt%Ce_3Si_2 exhibited up to 81% higher thermal conductivity than pure CeO_2 and even further thermal conductivity enhancement can

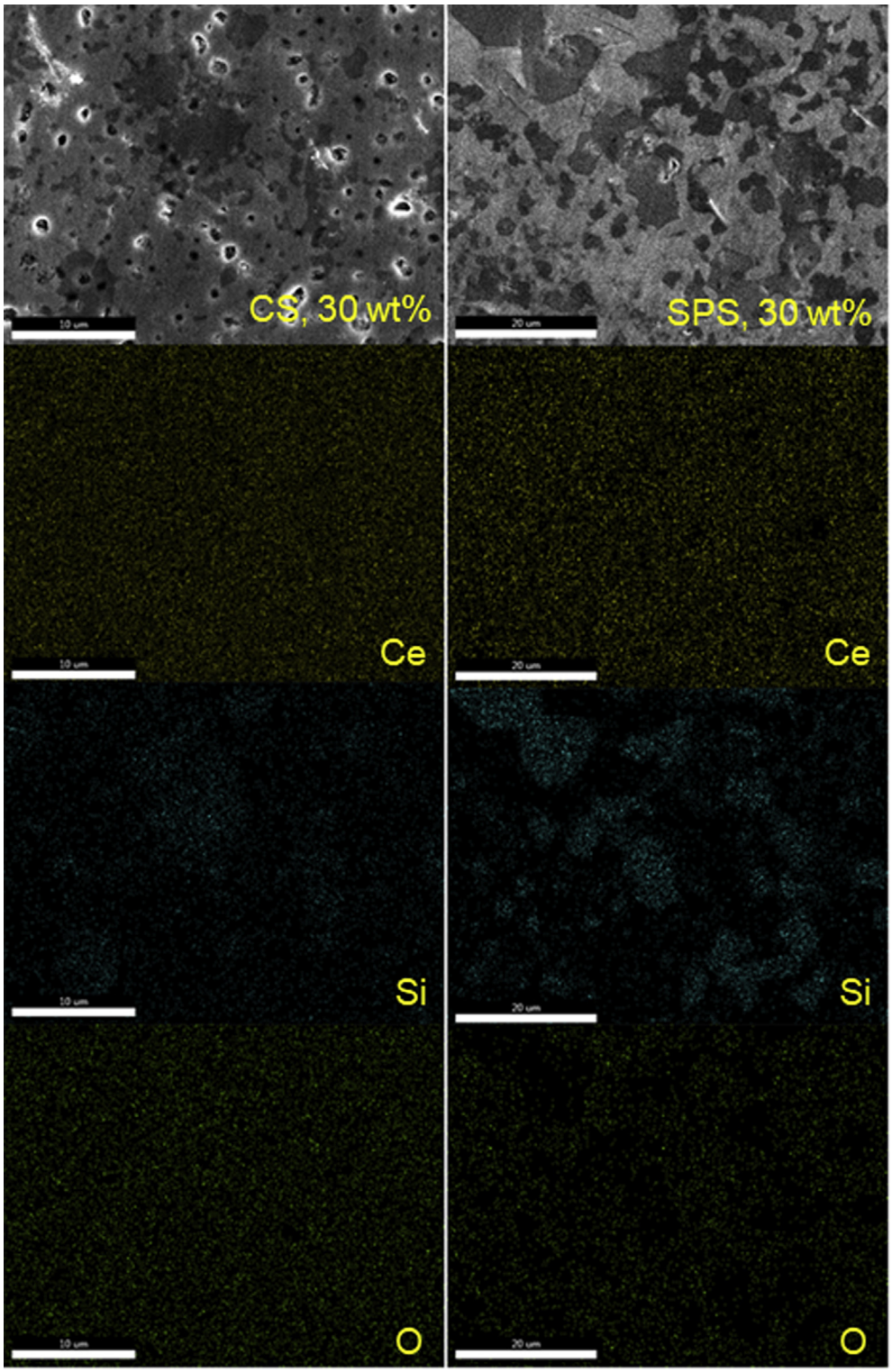

Fig. 9. EDS mapping image of CeO_2-30 wt%Ce_3Si_2 composite sintered by CS at 1600 °C for 6 h and SPS at 1400 °C for 10 min.

Table 1
Thermal conductivity and specific heat capacity of CeO_2–Ce_3Si_2 composite pellets sintered by SPS with varying Ce_3Si_2 composition.

Composition (wt%Ce_3Si_2)	0	10	30	50	100	0	10	30	50	100
Temperature (°C)	**Thermal conductivity (W/m-K)**					**Specific heat capacity (J/g-K)**				
50	4.54	3.62	3.46	3.92	5.53	0.36	0.42	0.38	0.37	0.36
100	3.88	3.33	3.24	3.74	5.66	0.39	0.42	0.38	0.38	0.36
150	3.35	3.09	3.06	3.62	5.76	0.40	0.43	0.39	0.39	0.36
200	2.94	2.89	2.92	3.52	5.85	0.41	0.44	0.40	0.39	0.37
250	2.67	2.73	2.81	3.41	5.89	0.42	0.44	0.40	0.40	0.37
300	2.47	2.58	2.73	3.32	5.84	0.43	0.45	0.41	0.40	0.37
350	2.28	2.47	2.60	3.23	5.90	0.43	0.45	0.42	0.40	0.38
400	2.15	2.36	2.52	3.14	6.02	0.44	0.46	0.42	0.41	0.38
450	2.02	2.26	2.46	3.07	6.12	0.44	0.47	0.43	0.41	0.38
500	1.92	2.18	2.37	3.00	6.23	0.44	0.47	0.43	0.42	0.39
550	1.84	2.11	2.31	2.94	6.35	0.44	0.48	0.44	0.42	0.39
600	1.75	2.05	2.25	2.88	6.47	0.44	0.48	0.44	0.42	0.39
650	1.68	2.01	2.21	2.84	6.61	0.45	0.49	0.45	0.43	0.40
700	1.61	1.97	2.18	2.80	6.74	0.45	0.49	0.45	0.43	0.40
750	1.56	1.95	2.14	2.78	6.90	0.45	0.50	0.46	0.43	0.40
800	1.57	1.93	2.12	2.77	7.13	0.46	0.50	0.47	0.44	0.40
850	1.52	1.93	2.11	2.76	7.46	0.46	0.51	0.47	0.44	0.40
900	1.48	1.92	2.09	2.76	7.93	0.46	0.52	0.48	0.45	0.40
950	1.49	1.93	2.09	2.75	8.36	0.46	0.52	0.48	0.46	0.40
1000	1.51	1.94	2.09	2.76	8.73	0.47	0.53	0.49	0.46	0.40

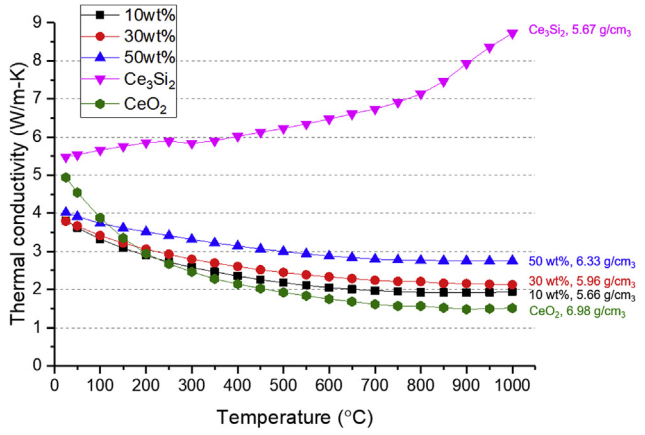

Fig. 10. Thermal conductivity of CeO_2-xCe_3Si_2 (x = 0, 10, 30, 50, and 100 wt%) sintered by SPS at 1400 °C for 10 min in vacuum. Part of the CeO_2 matrix was converted to Ce_2O_3 due to the reducible environment.

Table 2
Thermal conductivity change of CeO_2-xCe_3Si_2 (x = 10, 30, and 50 wt%) composite pellets compare to CeO_2, sintered by SPS at 1400 °C.

Temperature (°C)	Silicide composition (wt%)		
	10	30	50
	Thermal conductivity change (%)		
25	−22.84	−23.14	−18.61
100	−14.35	−12.08	−3.69
200	−1.68	4.29	19.51
300	4.80	13.32	34.53
400	9.45	21.38	46.00
500	13.26	27.81	56.09
600	17.67	34.30	65.27
700	22.28	39.64	73.67
800	23.21	40.27	76.81
900	29.47	46.31	85.78
1000	27.83	41.91	81.54

be expected from UO_2–U_3Si_2 composite due to stoichiometric UO_2 and higher U_3Si_2 density than UO_2.

Declaration of competing interest

The authors declare that they have no known competing financial interests or personal relationships that could have appeared to influence the work reported in this paper.

Acknowledgement

This research was supported by Basic Science Research Program through the National Research Foundation of Korea (NRF) funded by the Ministry of Science, ICT & Future Planning (No. NRF-2016R1A5A1013919).

References

[1] A.A.E. Abdelhameed, X.H. Nguyen, J. Lee, Y. Kim, Feasibility of passive autonomous frequency control operation in a soluble-boron-free small PWR, Ann. Nucl. Energy 116 (2018) 319–333.
[2] E.S. Solntceva, M.L. Taubin, V.I. Vybyvanets, I.E. Galyov, V.G. Baranov, O.V. Homyakov, A.V. Tenishev, Thermal conductivity of perspective fuel based on uranium nitride, Ann. Nucl. Energy 87 (2016) 799–802.
[3] J.T. White, A.T. Nelson, J.T. Dunwoody, D.D. Byler, D.J. Safarik, K.J. McClellan, Thermophysical properties of U_3Si_2 to 1773 K, J. Nucl. Mater. 464 (2015) 275–280.
[4] R. De Coninck, W. Van Lierde, A. Gijs, Uranium carbide: thermal diffusivity, thermal conductivity and spectral emissivity at high temperatures, J. Nucl. Mater. 57 (1975) 69–76.
[5] B.T.M. Willis, Structures of UO_2, UO_{2+x} and U_4O_9 by neutron diffraction, J. Phys. 25 (5) (1964) 431–439.
[6] A. Bumajdad, J. Eastoe, A. Mathew, Cerium oxide nanoparticles prepared in self-assembled systems, Adv. Colloid Interface Sci. 147–148 (2009) 56–66.
[7] B.A. Munitz, A.B. Gokhale, G.J. Abbaschian, The Ce-Si (cerium-silicon), System 10 (1989) 73–78.
[8] J. Rosales, Characterization of U_3Si_2 Surrogates to Predict U_3Si_2 Additive Manufactured Microstructures, 2018.
[9] R.K. Viswanadham, S.K. Mannan, S. Kumar, M.M. Laboratories, Mechanical alloying behavior in group V transition metal/silicon systems, Scripta Metall. 22 (1988) 1011–1014.
[10] S. Yagoubi, S. Heathman, A. Svane, G. Vaitheeswaran, P. Heines, J.C. Griveau, T. Le Bihan, M. Idiri, F. Wastin, R. Caciuffo, High pressure studies on uranium and thorium silicide compounds: experiment and theory, J. Alloys Compd. 546 (2013).
[11] J. Roleček, Š. Foral, K. Katovský, D. Salamon, A feasibility study of using CeO_2 as a surrogate material during the investigation of UO_2 thermal conductivity enhancement, Adv. Appl. Ceram. 116 (2017) 123–131.
[12] G.A. Alanko, B. Jaques, A. Bateman, D.P. Butt, Mechanochemical synthesis and spark plasma sintering of the cerium silicides, J. Alloys Compd. 616 (2014) 306–311.

[13] James Blanchard, D. Butt, M. Meyer, P. Xu, Development of Advanced High Uranium Density Fuels for Light Water Reactors, 2016.
[14] G.A. Alanko, D.P. Butt, Mechanochemical synthesis of uranium sesquisilicide, J. Nucl. Mater. 451 (2014) 243–248.
[15] FIZ Karlsruhe. Germany, ICSD - Inorganic Crystal Structure Database.
[16] Y. Kim, J. Park, J. Cleveland, Thermophysical Properties Database of Materials for Light Water Reactors and Heavy Water Reactors, 2006.
[17] D.R. Mullins, The Surface Chemistry of Cerium Oxide, 2014.
[18] R.A. Prasad, Spark Plasma Sintering of Cerium Dioxide and its Composites, 2017.
[19] D. Galusek, K. Ghillányová, Ceramic oxides, Ceram. Sci. Technol. 2 (2010). Mater. Prop.
[20] T. Zhang, P. Hing, H. Huang, J. Kilner, Sintering study on commercial CeO_2 powder with small amount of MnO_2 doping, Mater. Lett. 57 (2002) 507–512.
[21] Y.C. Zhou, Hydrothermal synthesis and sintering of ultrafine CeO_2 powders, J. Mater. Res. 8 (1993) 1680–1686.
[22] P.A. Lessing, Oxidation Protection of Uranium Nitride Fuel Using Liquid Phase Sintering, 2012.
[23] K.D. Johnson, A.M. Raftery, D.A. Lopes, J. Wallenius, Fabrication and microstructural analysis of UN-U3Si2 composites for accident tolerant fuel applications, J. Nucl. Mater. 477 (2016) 18–23.
[24] J.T. White, A.W. Travis, J.T. Dunwoody, A.T. Nelson, Fabrication and thermophysical property characterization of UN/U_3Si_2 composite fuel forms, J. Nucl. Mater. 495 (2017) 463–474.
[25] G. Lee, E.A. Olevsky, C. Manière, A. Maximenko, O. Izhvanov, C. Back, J. Mckittrick, Effect of electric current on densification behavior of conductive ceramic powders consolidated by spark plasma sintering Acta Materialis Effect of electric current on densi fi cation behavior of conductive ceramic powders consolidated by spark plasma sintering, Acta Mater. 144 (2017) 524–533.
[26] Y. Achenani, M. Saâdaoui, A. Cheddadi, G. Bonnefont, G. Fantozzi, Finite element modeling of spark plasma sintering : application to the reduction of temperature inhomogeneities , case of alumina, JMADE 116 (2016) 504–514.
[27] E.S. Folias, M. Hohn, T. Nicholas, Predicting crack initiation in composite material systems due to a thermal expansion mismatch, Int. J. Fract. 93 (1998) 335–349.
[28] F. Delale, H. Boduroglu, Effect of thermal expansion anisotropy on microcracking in ceramic composites, Eng. Fract. Mech. 39 (1991) 45–60.
[29] J. Williams, Sintering of uranium oxides of composition UO_2 to U_3O_8 in various atmospheres, J. Nucl. Mater. 1 (1959) 28–38.